

InP- and graphene-based grating-gated transistors for tunable THz and mm-wave detection

R. E. Peale^{*a}, Nima Nader Esfahani^a, Christopher J. Fredricksen^a, Gautam Medhi^a, Justin W. Cleary^b, Joshua Hendrickson^b, Walter R. Buchwald^c, Himanshu Saxena^d, Oliver J. Edwards^d, Michael S. Lodge^e, Ben D. Dawson^e, and M. Ishigami^e

^aDepartment of Physics, University of Central Florida, Orlando FL, USA 32816;

^bAir Force Research Laboratory, Sensors Directorate, Hanscom AFB MA, USA 01731;

^cSolid State Scientific Corporation, 12 Simon St. Nashua, NH 03060

^dZyberwear Inc., Ocoee FL, USA

^eDepartment of Physics and Nanoscience Technology Center, University of Central Florida, Orlando, FL 32816

ABSTRACT

Tunable resonant absorption by plasmons in the two-dimensional electron gas (2DEG) of grating-gated HEMTs is known for a variety of semiconductor systems, giving promise of chip-scale frequency-agile THz imaging spectrometers. We present our calculations of transmission spectra and resonant photoresponse due to plasmons in InP- and graphene-based HEMTs at millimeter and THz wavelengths. Our experimental approach to measurement of electrical response is also described. Potential applications include man-portable or space-based spectral-sensing.

Keywords: HEMT, Plasmon, terahertz, millimeter wave

1. INTRODUCTION

Grating gated MOSFETs and HEMTs display tunable resonant absorption of THz radiation [1, 2, 3]. In some cases, this absorption gives rise to a resonant change in channel conductance [4], which is potentially the basis for a tunable terahertz detector. Such would have applications in spectral sensing and imaging. This paper presents theoretical predictions, design and experimental considerations, and first experimental results for HEMTs based on the InP materials system and on graphene.

2. INDIUM PHOSPHIDE BASED GRATING-GATED HEMTS

Tunable resonant plasmon absorption in an InP-based HEMT was observed [1], but an associated resonant photoresponse using a free electron laser as a source was not [5]. These first devices had a substantial non-resonant and non-linear photoresponse, which, together with the significant shot-to-shot intensity variations and low duty cycle of the FEL, made it impossible to observe the sought after resonant photoresponse. To improve our chances of observing a weak photoresponse, we have redesigned our device to have mm-wave resonances, since available mm-wave backward wave oscillators have high intensity stability, high frequency agility, provide frequency modulation to allow lock-in detection, and are table-top devices. By this means, we anticipate being able to detect a photoresponse, after which there will be opportunity to optimize the response.

First generation InP-based HEMT devices (Fig. 1), characterized by Fourier spectroscopy, revealed a spectrum of gate-tunable plasmon absorption resonances and their harmonics. However, these were found to occur at 2-3 x lower frequency than predicted by the dispersion relation

$$\omega_p^2(x=d) = \frac{e^2 n_s q_n}{m^* \epsilon_0 (\epsilon_s + \epsilon_d \coth(q_n d))} \quad , \quad (1)$$

where e is the electron charge, n_s the sheet charge density, q the grating wavevector, m^* the effective mass, ϵ_0 the vacuum permittivity, ϵ_s the permittivity of substrate below the 2DEG, ϵ_d that above, and d the distance between gate and 2DEG. The resonances and their harmonics could be adequately explained if a “virtual gate” (large electron concentration) existed 4.5 nm above the 2DEG [6-8]. Consequently, we have also chosen a different InP-based HEMT layer structure that avoids the such virtual gate. Two new devices were prepared, PLS023C and PLS023A, with grating periods of 10 and 0.5 μm , for mm-wave and FTIR experiments, respectively. The layer structure is the same as the device studied in [8], which is presented in Fig. 1 together with the electron density distribution as determined by Silvaco Atlas 2-D device simulator (FEM analysis software). Here we report calculations of their plasmon absorption spectra. Also we predict the resonant electrical response of PLS023C devices to frequency modulated BWO millimeter-wave radiation with lock-in amplification of Source-Drain current. The top side micrograph of the mm-wave sample is presented in Fig. 1 (right). A lamellar grating with 10 micron period covers the gate.

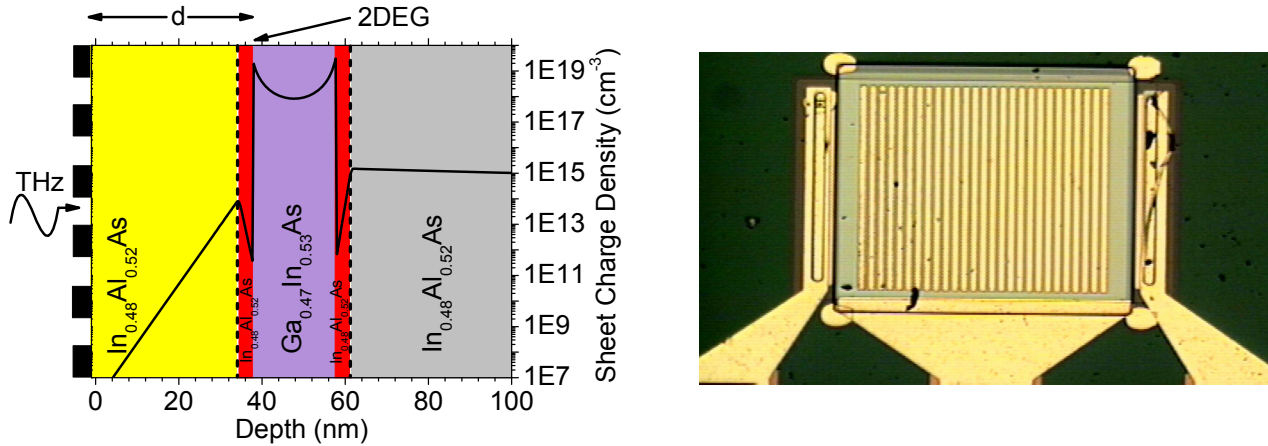


Fig. 1. (left) Schematic of layer structure and calculated electron concentration of PLS023 HEMT device with A: Undoped $\text{In}_{0.52}\text{Al}_{0.48}\text{As}$, Dash line: Si δ -doped layer, B: $\text{In}_{0.52}\text{Al}_{0.48}\text{As}$ Setback, C: $\text{In}_{0.53}\text{Ga}_{0.47}\text{As}$ Channel, D: Undoped $\text{In}_{0.52}\text{Al}_{0.48}\text{As}$, Dash Line: Second Si δ -doped layer and E: Undoped $\text{In}_{0.52}\text{Al}_{0.48}\text{As}$ Buffer. (right) Microscopic image of 2nd-generation device metallization. Grating periodicity $a = 10\mu\text{m}$ and $5\mu\text{m}$, metallization ratio $t/a = 0.3$

Calculation of the plasmon resonance spectrum by the method of [9] requires knowledge of the temperature dependent sheet charge density n_s and relaxation time τ . These are determined from IV and transfer curves. The saturated source-drain current $I_{\text{sd-sat}}$ vs. gate bias V_g is fit [1] to determine mobility μ and carrier concentration n_d , from which are determined n_s and τ . The device is cooled in a temperature-controlled cryostat. The negative gate bias is computer controlled. Source and Drain are connected to Keithley 2400 source meter to apply voltage to the source and to measure the drain current. The measured IV Curves for $T = 295\text{ K}$ and 4 K are presented in Fig. 2 (left). $I_{\text{sd-sat}}$ vs. V_g curves are plotted in Fig. 2 (right) as symbols for different temperatures. The curves are fits [1], where the fit parameters n_d and μ allow determination of n_s and τ , which are plotted in Fig. 3.

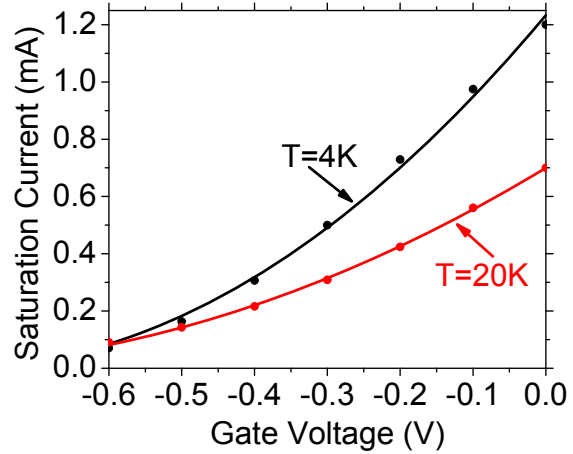
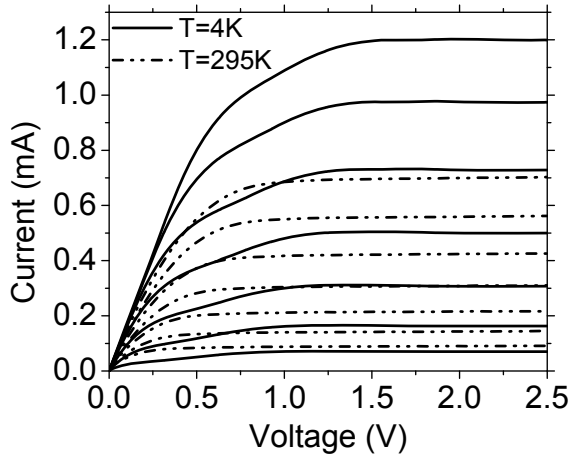


Fig. 2 (left). Measured IV-Curves for PLS023 samples with: $a = 10 \mu\text{m}$ and $5 \mu\text{m}$ and $t/a = 0.3$ at $T = 295 \text{ K}$ and $T = 4 \text{ K}$. (right) $I_{\text{sd-sat}}$ vs V_g data (symbols) and fits (lines).

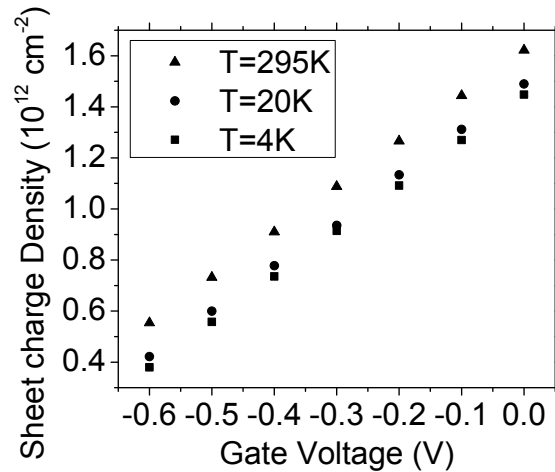
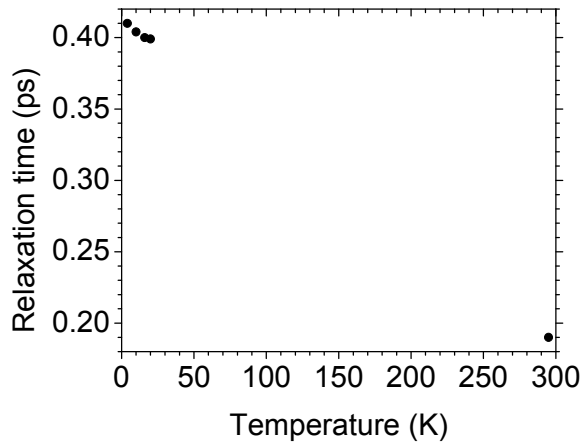


Fig. 3. (left) Relaxation time vs temperature. (Right) Sheet charge density as a function of gate voltage for different temperatures.

Figure 4 (left) presents transmission spectra calculated for PLS023C at $T = 4 \text{ K}$ at $V_g = 0 \text{ V}$, and the plasmon resonance appears at $\sim 10 \text{ cm}^{-1}$. Figure 4 (right) represents the spectrum of PLS023A, for which the fundamental plasmon occurs at 100 cm^{-1} . To measure the latter spectrum, we have interfaced a Hyperion IR microscope to a 4K Si-bolometer, an optical cryostat, and a Bruker FTIR. For PLS023C, we will seek resonance mm-wave photoresponse using and FM BWO with lock-in detection, as described in [8].

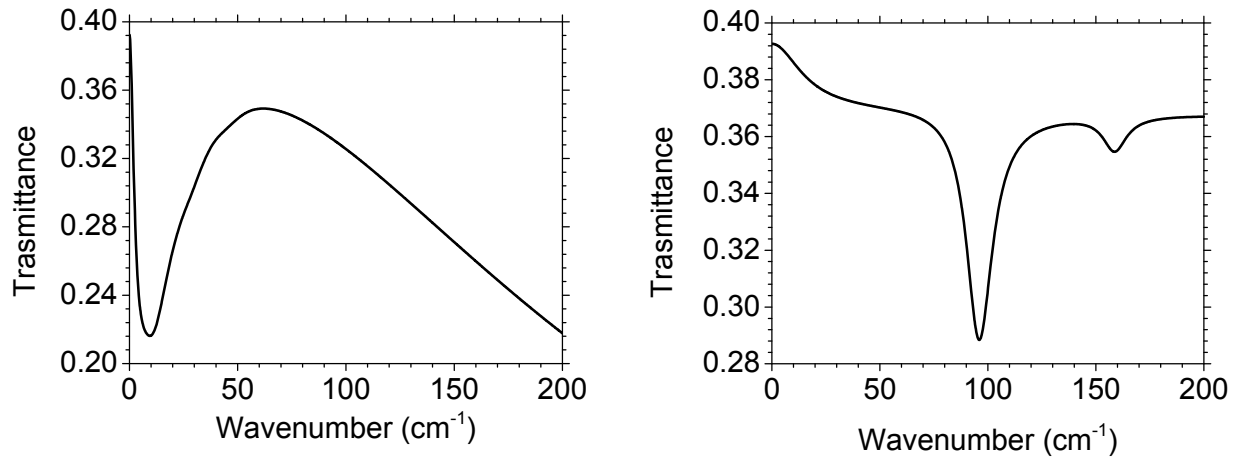


Fig. 4 (left). Transmission spectrum for PLS023C with $a = 10$ micron and gap-to-period ratio of $t/a = 0.3$. **(Right)** Transmission spectrum for PLS023A with $a = 0.5\mu\text{m}$ and $t/a = 0.3$.

Resonances shift with gate-bias, as shown in calculations for PLS023C (Fig. 5, left). Increasing the negative gate voltage decreases the sheet charge density, which shifts the band to lower wavenumbers while making it shallower. The 40-110 GHz ($1.3 - 3.7 \text{ cm}^{-1}$) range of our BWO sources is too narrow to sweep over the full width of mm-wave plasmon resonances. The BWO ranges are plotted together with an expanded view of the spectrum in Fig. 5 (right), where the useful feature to note is the decrease in dT/df as more negative gate bias is applied.

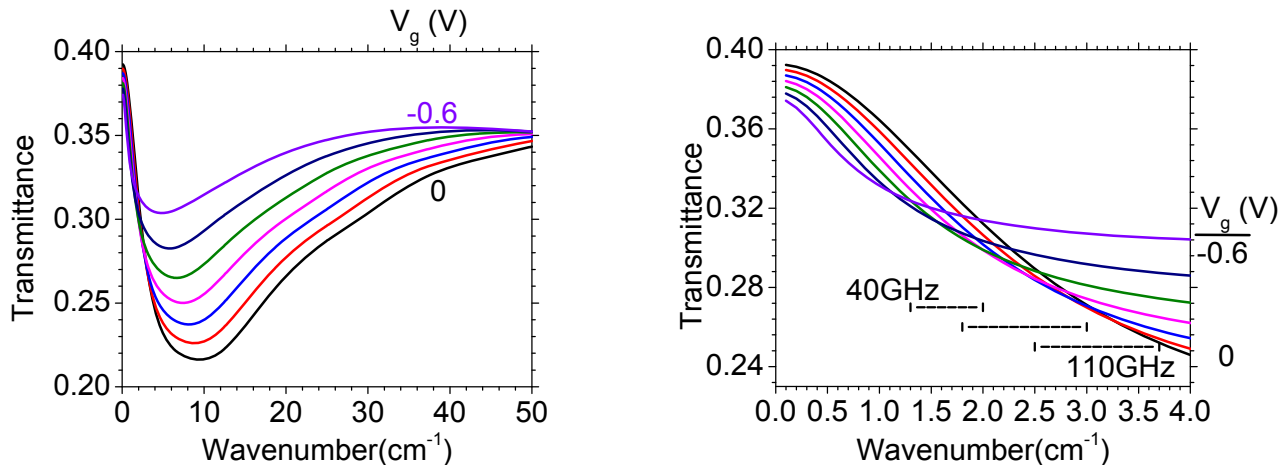


Fig. 5 (left). Calculated transmittance spectra as a function of gate voltage for PLS023C HEMT. **(right)** Calculated transmittance spectra together with ranges of our three BWOs ($1.3 - 3.7 \text{ cm}^{-1}$) for PLS023C. Horizontal bars indicate the ranges of our three BWO heads. In both plots, the extremes of the V_g range are indicated next to their corresponding curve, which each curve differing from its neighbors by 0.1 V .

We frequency modulate the BWO with modulation amplitude Δf and synchronously lock-in amplify the measured source-drain current I_{SD} . Supposing an effect on channel conductance due to the absorption by plasmons, whose absorptance $A = 1 - T - R$, then the lock-in output will be proportional to $|(dT/df)|\Delta f$. Fig. 6 presents dT/df from the transmittance spectra. A record of lock-in output for different V_g values should produce a set of points corresponding to a vertical slice through the calculated curves in Fig. 6. By choosing different center frequencies, we should be able to reproduce the complete curves shown in Fig. 6 over the BWO ranges indicated.

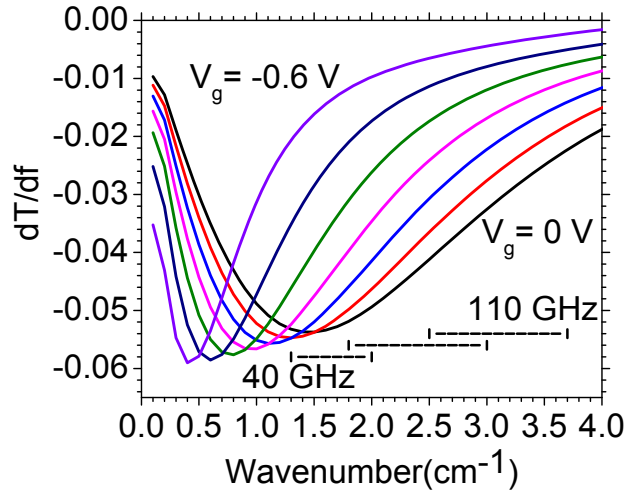


Fig. 6. Calculated dT/df spectra in BWO range (1.3 – 3.7 cm^{-1}) for PLS023C. The extremes of the V_g range are indicated next to their corresponding curve, with each curve differing from its neighbors by 0.1 V. Horizontal bars indicate our BWO ranges.

3. GRAPHENE

Graphene, a single layer of graphite, possesses extraordinary field effect mobility reaching 20,000 $\text{cm}^2/\text{V}\cdot\text{sec}$ at room temperature and its electronic density of states vanishes at the Fermi level [11]. As such, graphene-based HEMT plasmonics can have highly tunable and sharp plasmon resonance. Furthermore, graphene is lightweight, optically transparent, and intrinsically flexible. With these exceptional properties, the adaption of graphene in the HEMT-based plasmonics technology will enhance its utility in lightweight, discreet, and flexible electronics.

Previous study [12] on plasmons in graphene have not exploited the large tunability offered using the device configuration explored in the HEMT-based plasmonic technology. Using a semiclassical model for the conductivity of graphene, the plasmon dispersion relation of free standing graphene is given by [13]

$$q(\omega) = \frac{\pi\hbar\epsilon_0}{e^2 E_F} \left(1 + \frac{i}{\tau\omega} \right) \omega^2, \quad (2)$$

where e is the electron charge, and E_F denotes the Fermi energy of graphene. This relation is valid when $E_F \gg k_B T$. The plasmon dispersion in graphene can be tuned by varying its Fermi energy. Just as in the case of the InP-based HEMT devices described above, a grating can be used to efficiently couple light into plasmons in graphene and also to electrostatically tune the electronic density of states and, thus, the plasmon frequency.

The schematic of a device is shown in the inset of Figure 7. Large graphene with a lateral dimension reaching over 1 cm will be grown using chemical vapor deposition (CVD) and transferred onto a high resistivity silicon substrate. PMMA will then be deposited on top of the graphene and overexposed with an electron beam to create a hardened dielectric layer. A metal grating will then be deposited onto the PMMA dielectric and will serve as the gate electrode that will vary the carrier density and, thus, the Fermi energy of graphene.

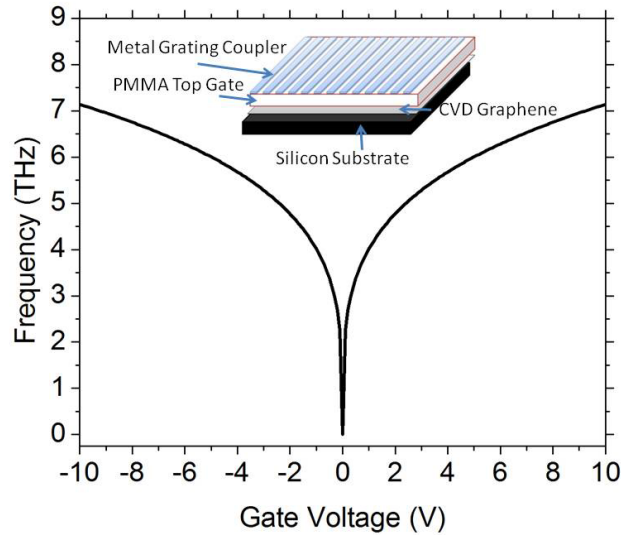


Figure 7: Calculated resonance peak vs. gate voltage for a proposed graphene HEMT with grating gate. The device parameters are $a = 500$ nm, $d_{\text{PMMA}}=60$ nm, and $E_F = 0$ V at $V_g = 0$ V (undoped graphene).

Figure 7 shows the calculated dependence of graphene plasmons with an example metal grating gate with a grating periodicity of 500 nm, a grating width of 400 nm, and gate dielectric thickness of 60 nm. Using the same semiclassical approach as above and following the previous results by Zheng et al. [9], the non-retarded dispersion for plasmons in graphene separated by d from a perfectly conducting gate can be written as

$$\omega_n^2 = \frac{e^2 E_F q_n}{\pi \hbar^2 \epsilon_0 (\epsilon_s + \epsilon_d \coth(q_n d))}, \quad (3)$$

where $q_n = (2\pi/a)n$, with gate grating period $a = 500$ nm, integer n , $\epsilon_s = 11.68$, and $\epsilon_d = 3.3$ (permittivities of silicon and PMMA, respectively). For the frequency of the fundamental resonance ($n = 1$) in Figure 7, graphene is assumed to be undoped (i.e. $E_F = 0$ V when $V_g = 0$ V). The dispersion relation derived here may not be accurate at $E_F = 0$, but the behavior of the plasmon resonance with applied gate voltage should still be valid elsewhere as stated previously.

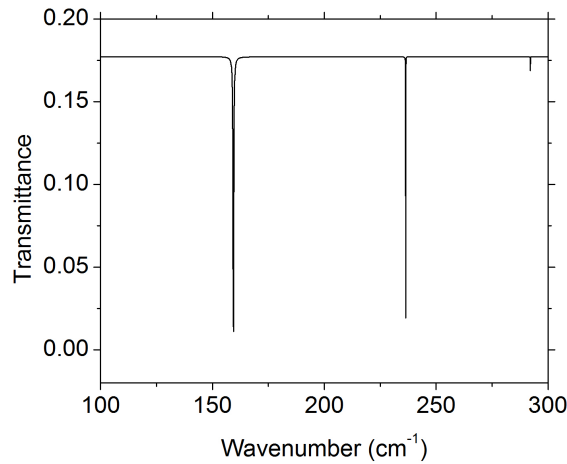


Figure 8: The calculated transmission spectrum of graphene corresponding to a gate voltage of 2 V from figure 7, with $a = 500$ nm and gap-to-period ratio of $t/a = 0.2$.

Figure 8 presents a calculated transmission spectrum of graphene based on the previous analysis on the HEMT plasmonics [9]. For this calculation, we chose a Fermi energy of 0.09 eV, corresponding to a carrier concentration of $n = 6.08 \times 10^{11} \text{ cm}^{-2}$. This value for Fermi energy corresponds to an applied gate voltage of 2 V from Figure 7. The relaxation time is proportional to the mobility, here assumed to be $\mu = 10000 \text{ cm}^2/\text{V-s}$, and is calculated as

$$\tau = \frac{\mu \hbar \sqrt{n \pi}}{e v_F} = 9 \times 10^{-10} \text{ s}, \quad (4)$$

where v_F is the Fermi velocity and equals $1.1 \times 10^6 \text{ m/s}$. The resonance peaks are very sharp, owing to the high carrier mobility and long relaxation time. As such, graphene is an ideal material for HEMT plasmonics applications.

It is important to understand the role of the substrate on the graphene, as this can influence the density and mobility of the charge carriers [14]. Figure 9 shows the measured transmittance of graphene on a silicon substrate. The broad dip in transmittance between 400 and 500 cm^{-1} is most likely due to an oxide layer on the silicon. The decrease in transmittance at long wavelengths gives evidence for free carrier absorption, which implies that the as-deposited graphene is not charge neutral, as assumed in our derivation of Figure 7. Thus, the choice of materials for both the substrate and the top dielectric layer will affect the range of Fermi energies available for attainable gate voltages, giving another method to tailor graphene-based HEMT plasmonic devices to a range of desired wavelengths.

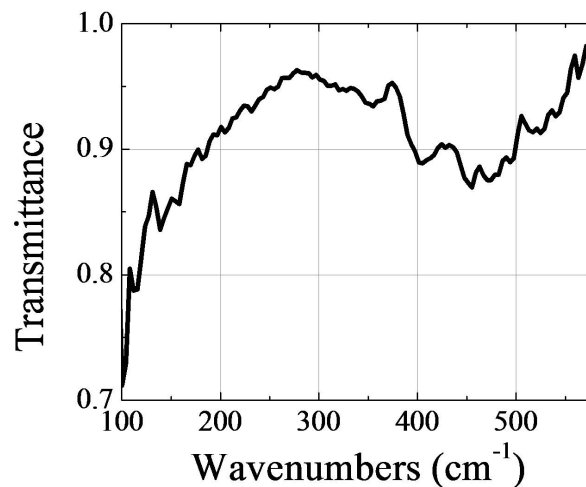


Figure 9: Transmittance of graphene on silicon. The CVD grown sample had a 1 cm^2 cross section. The spectrum was collected using a Fourier spectrometer with global source, mylar pellicle beamsplitter, and room temperature pyroelectric detector. At longer wavelengths the transmission decreases due to free carrier absorption.

4. SUMMARY

InGaAs/InP HEMT devices each fabricated with grating-gate period designed to allow coupling of mm-wave radiation to resonant plasmon absorption. Expectations for the detection of a corresponding electrical response to mm-wave radiation from frequency modulated BWOs were calculated. Furthermore, we have also explored the possibility of using CVD-grown graphene in the HEMT-based plasmonic devices and find that the use of graphene will enhance the utility of HEMT-based plasmonics in lightweight, transparent, and flexible electronics.

5. ACKNOWLEDGMENTS

This work was supported by AFOSR grant FA95501010030, Program Manager Gernot Pomrenke. BDD and MI acknowledge the support by the Intelligence Community Postdoctoral Fellowship Program.

REFERENCES

- [1] H. Saxena, R. E. Peale and W. R. Buchwald, "Tunable two-dimensional Plasmon resonances in an InGaAs/InP HEMT", *J. Appl. Phys.* **105**, 113101 (2009).
- [2] S. J. Allen, D. C. Tsui, and R. A. Logan, "Observation of the Two-Dimensional Plasmon in Silicon Inversion Layers." *Phys. Rev. Lett.* **38**, 980 (1977).
- [3] A. V. Muravjov, D. B. Veksler, X. Hu, R. Gaska, N. Pala, H. Saxena, R. E. Peale, M.S. Shur "Resonant terahertz absorption by plasmons in grating-gate GaN HEMT structure" *Proc. SPIE* 7311-12 (2009).
- [4] X. G. Peralta, S. J. Allen, M. C. Wanke, N. E. Harff, J. A. Simmons, M. P. Lilly, J. L. Reno, P. J. Burke, and Eisenstein, "Terahertz photoconductivity and plasmon modes in double-quantum-well field-effect transistors", *Appl. Phys. Lett.* **81**, 1627 (2002).
- [5] R. E. Peale, H. Saxena, W. R. Buchwald, G. C. Dyer, S. J. Allen, Jr. "Tunable THz plasmon resonances in InGaAs/InP HEMT," *Proc. SPIE* 7311-17 (2009).
- [6] R. E. Peale, H. Saxena, W. R. Buchwald, G. Aizin, A. V. Muravjov, D. B. Veksler, N. Pala, X. Hu, R. Gaska, M. S. Shur, "Grating-gate tunable plasmon absorption in InP and GaN based HEMTs," *Proc. SPIE* 7467-25 (2009).
- [7] J. W. Cleary, R. E. Peale, H. Saxena, and W. R. Buchwald. "Investigation of plasmonic resonances in the two-dimensional electron gas of an InGaAs/InP high electron mobility transistor." *Proc. SPIE* 8023-33 (2011).
- [8] N. Nader Esfahani, R. E. Peale, J. Cleary, W. R. Buchwald. "Plasmon resonance response to millimeter-waves of grating-gated InGaAs/InP HEMT," *Proc. SPIE* 8023-27 (2011)
- [9] A. H. Macdonald, L. Zheng, W. L. Schaich, "Theory of two-dimensional grating couplers." *Phys. Rev. B* 41, 8493 (1990)
- [10] W. R. Buchwald, H. Saxena, R. E. Peale, "Tunable Far-IR Detectors/Filters Based on Plasmons in Two Dimensional Electron Gases in InGaAs/InP Heterostructures," *Proc. SPIE* 6678-32 (2007).
- [11] A. K. Geim and K. S. Novoselov, "The rise of graphene", *Nature Materials*, 6, 183 (2007)
- [12] T. J. Echtermeyer, L. Britnell, P. K. Jasnós, A. Lombardo, R. V. Gorbachev, A. N. Grigorenko, A. K. Geim, A. C. Ferrari, K. S. Novoselov, "Strong plasmonic enhancement of photovoltage in graphene", *Condensed matter preprint archive*, 1107.4176 (2011)
- [13] M. Jablan, H. Buljan and M. Soljačić, "Plasmonics in graphene at infrared frequencies", *Phys. Rev. B* 80, 245435 (2009).
- [14] J. Y. Kim, C. Lee, S. Bae, K. S. Kim, B. H. Hong and E. J. Choi, "Far-infrared study of substrate-effect on large scale graphene", *Appl. Phys. Lett.* 98, 201907 (2011)